



HAL
open science

Hazardous explosive eruptions of a recharging multi-cyclic island arc caldera

Jonas Preine, Jens Karstens, Christian Hübscher, Timothy H. Druitt, Steffen Kutterolf, Paraskevi Nomikou, Michael Manga, Ralf Gertisser, Katharina Pank, Sarah Beethe, et al.

► **To cite this version:**

Jonas Preine, Jens Karstens, Christian Hübscher, Timothy H. Druitt, Steffen Kutterolf, et al.. Hazardous explosive eruptions of a recharging multi-cyclic island arc caldera. *Nature Geoscience*, 2024, 17, pp.323-331. 10.1038/s41561-024-01392-7. insu-04730636

HAL Id: insu-04730636

<https://insu.hal.science/insu-04730636v1>

Submitted on 10 Oct 2024

HAL is a multi-disciplinary open access archive for the deposit and dissemination of scientific research documents, whether they are published or not. The documents may come from teaching and research institutions in France or abroad, or from public or private research centers.

L'archive ouverte pluridisciplinaire **HAL**, est destinée au dépôt et à la diffusion de documents scientifiques de niveau recherche, publiés ou non, émanant des établissements d'enseignement et de recherche français ou étrangers, des laboratoires publics ou privés.



Distributed under a Creative Commons Attribution 4.0 International License

Hazardous explosive eruptions of a recharging multi-cyclic island arc caldera

Received: 27 September 2023

Accepted: 2 February 2024

Published online: 25 March 2024

 Check for updates

Jonas Preine ¹✉, Jens Karstens ², Christian Hübscher ¹, Tim Druitt ³, Steffen Kutterolf ², Paraskevi Nomikou ⁴, Michael Manga ⁵, Ralf Gertisser ⁶, Katharina Pank ², Sarah Beethe ⁷, Carole Berthod ⁸, Gareth Crutchley ², Iona McIntosh ⁹, Thomas Ronge ¹⁰, Masako Tominaga ¹¹, Acacia Clark ¹², Susan DeBari ¹³, Raymond Johnston ¹⁴, Zenon Mateo ¹⁰, Ally Peccia ¹⁵, Christopher Jones ¹⁶, Günther Kletetschka ^{17,18}, Abigail Metcalfe ³, Alexis Bernard ¹⁹, Hehe Chen ²⁰, Shun Chiyonobu ²¹, Tatiana Fernandez-Perez ²², Kumar Batuk Joshi ²³, Olga Koukousioura ^{24,25}, Molly McCanta ²⁶, Antony Morris ²⁷, Paraskevi Polymenakou ²⁸, Adam Woodhouse ^{29,30}, Yuzuru Yamamoto ³¹, Kuo-Lung Wang ^{32,33}, Hao-Yang Lee ³², Xiaohui Li ³⁴ & Dimitrios Papanikolaou ⁴

Caldera-forming eruptions of silicic volcanic systems are among the most devastating events on Earth. By contrast, post-collapse volcanic activity initiating new caldera cycles is generally considered less hazardous. Formed after Santorini's latest caldera-forming eruption of ~1600 BCE, the Kameni Volcano in the southern Aegean Sea enables the eruptive evolution of a recharging multi-cyclic caldera to be reconstructed. Kameni's eruptive record has been documented by onshore products and historical descriptions of mainly effusive eruptions dating back to 197 BCE. Here we combine high-resolution seismic reflection data with cored lithologies from International Ocean Discovery Program Expedition 398 at four sites to determine the submarine architecture and volcanic history of intra-caldera deposits from Kameni. Our shore-crossing analysis reveals the deposits of a submarine explosive eruption that produced up to 3.1 km³ of pumice and ash, which we relate to a historical eruption in 726 CE. The estimated volcanic explosivity index of magnitude 5 exceeds previously considered worst-case eruptive scenarios for Santorini. Our finding that the Santorini caldera is capable of producing large explosive eruptions at an early stage in the caldera cycle implies an elevated hazard potential for the eastern Mediterranean region, and potentially for other recharging silicic calderas.

Large silicic volcanic systems have the potential to create catastrophic caldera-forming eruptions, capable of impacting human societies on a global scale¹. Many silicic caldera systems are thought to follow recurrent evolutionary paths^{2,3}. Caldera cycles typically comprise

(1) rejuvenation and recharge by new magmas after caldera collapse associated with small and frequent eruptions, and (2) a build-up stage with few relatively small eruptions of differentiated magmas culminating in (3) a climactic eruption associated with large-scale magma

A full list of affiliations appears at the end of the paper. ✉ e-mail: jonas.preine@uni-hamburg.de

withdrawal and caldera collapse^{2,3}. Despite their much smaller magnitudes, eruptions during stages 1 and 2 at calderas, as seen, for example, at Campi Flegrei⁴, Taupo⁵, Rabaul⁶ or Nisyros⁷, can present a major hazard to populations and infrastructure. Therefore, understanding the timing for the magmatic system beneath a caldera to reactivate and produce new explosive activity after an initial caldera-forming event is crucial. However, since the products from eruptions early in a caldera cycle are commonly buried deep within intra-caldera fill, our knowledge about them is underdeveloped, and the time needed for the system to build up to hazardous explosive events is poorly understood.

Considered to be a typical example of a multi-cyclic caldera, Santorini is part of the South Aegean Volcanic Arc in the eastern Mediterranean (Fig. 1a). Santorini's caldera cycles are characterized by extended periods of effusive to mildly explosive intra-caldera volcanism between caldera-forming events^{8–10}. Activity at Santorini first began ~650 ka, and since half a million years ago there have been numerous Plinian eruptions, five of which are believed to have generated calderas^{8,11}. The latest caldera-forming eruption of Santorini occurred ~1600 BCE, discharging a dense-rock equivalent (DRE) of silicic magma and rock fragments of $34.5 \pm 6.8 \text{ km}^3$, which possibly contributed to the demise of the Minoan civilization^{12,13}. Post-collapse volcanism resumed with the build-up of the intra-caldera Kameni Volcano, marking the beginning of a new caldera cycle^{10,14}.

Kameni Volcano is a largely submarine edifice in the centre of the caldera (Fig. 1b–d) with two summits forming the islands of Palea Kameni and Nea Kameni^{15,16} (Fig. 1c). It separates the caldera into a northern and a southern basin, which have maximum depths of 385 m and 290 m, respectively¹⁶ (Fig. 1b,d). Historical descriptions provide a record of multiple eruptions of Kameni Volcano that date back to 197 BCE and continued until 1950 CE^{8,15,17}. Since then, the volcano has been dormant except for a phase of seismo-volcanic unrest in 2011–2012 CE¹⁸. Previous seismic reflection studies of the caldera infill identified three stratigraphic units, interpreted as composed either of (1) Minoan and pre-Minoan ignimbrites¹⁹, (2) mixed Minoan and post-Minoan deposits²⁰ or (3) entirely post-Minoan deposits^{13,21}.

International Ocean Discovery Program (IODP) Expedition 398 drilled into the marine basins of the Santorini caldera²² (Fig. 1b,c). Four coring sites reveal the eruption history of Kameni Volcano. Here, we integrate recovered lithologies with high-resolution seismic data to map the distribution and volume of individual units. We relate these units to lava flows from Kameni Volcano to reconstruct its evolution, identifying an unexpectedly large explosive eruption in historical times.

Lithologies of intra-caldera deposits

IODP Expedition 398 cored two sites in each of Santorini caldera's southern (U1594, U1595) and northern (U1596, U1597) basins (Fig. 1b). Challenging drilling conditions prevented penetration of the acoustic basement and recovery rates decreased with depth (Fig. 2). The retrieved material was unlithified sediment, dominated by volcaniclastic material with minor amounts of tuffaceous mud. Five lithologic units (L1–L5) were identified, with the lowermost units L3–L5 solely obtained at Site U1595 (Fig. 2). At all sites, unit L1 extends from the seafloor down to ~20 metres below seafloor (mbsf), comprising mainly well-sorted, partly decimetre-thick ash with one additional metre-thick lapilli-ash interval (Figs. 2 and 3a). The transition between units L1 and L2 is marked by the occurrence of moderate to highly vesicular pumice lapilli (Fig. 3a). Unit L2 (~20–55 mbsf) consists of volcanic material that grades upwards from pumice lapilli to lapilli-ash (Fig. 2), with pumice lapilli up to 5 cm in diameter (Fig. 3a). At Site U1595, unit L3 comprises numerous intervals of intercalated ash and tuffaceous mud, extending to ~60 mbsf (Figs. 2 and 3a). Unit L4 extends to ~100 mbsf and consists of heterogeneous volcanic lithologies, including lithic gravels and sands, with lithic blocks (Figs. 2 and 3a). Unit L5, extending to at least ~126 mbsf, contains pumice lapilli, red volcanic ash and lithics; the bottom of this unit was not recovered (Figs. 2 and 3a).

Seismostratigraphy and correlation to core data

The high-resolution seismic profile shown in Fig. 3c crosses the Santorini caldera and all four drill sites. Following previous studies, we subdivide the caldera infill into three seismic units, numbered S1–S3 from the top to the incoherent acoustic basement^{13,20,21} (Fig. 3c and Extended Data Figs. 1–3). Unit S1 represents the shallowest infill in both basins and is characterized by incoherent low-amplitude reflections and a flat upper surface (Fig. 3c). The top of unit S2 marks an unconformity with undulating topography. The internal reflections of unit S2 are subparallel and have higher amplitudes than those of unit S1 (Fig. 3c). The boundary between units S2 and S3 is marked by a distinct high-amplitude reflection, which is conformable in the southern basin but unconformable in the northern basin (Fig. 3d,e). Towards Kameni Volcano, this boundary coincides with a high-amplitude reflection marking the top of an incoherent seismic subunit that pinches out distally from the edifice and is associated with acoustic blanking below (Fig. 3d,e). Unit S3 has a roughly constant thickness in the southern basin, whereas it thickens strongly towards Kameni Volcano in the northern basin and displays divergent internal reflections (Fig. 3e). Unit S3 fills the topographic low of the underlying acoustic basement, displaying clear onlap structures (Fig. 3d,e). Acoustic blanking beneath Kameni Volcano prevents determining the extent of unit S3 below the centre of the caldera (Fig. 3d,e).

Using shipboard P-wave velocity and density measurements of the recovered cores, we correlate the recovered material to seismic reflections integrating the cored lithologic units with the seismic units. At all four sites, we correlate seismic unit S1 with lithologic unit L1 (Fig. 3d,e) and seismic unit S2 with lithologic unit L2 (Fig. 3d,e). Lithologic unit L3 represents a thin (~5 m) interval that underlies the high-amplitude reflection separating seismic units S2 and S3 (Fig. 3d,e). Towards Kameni Volcano, this high-amplitude reflection marks the top of the incoherent subunit whose base is marked by the dashed red lines in Fig. 3d,e. Lithologic units L3–L5 can be correlated with seismic unit S3. Low recovery in lithologic units L4 and L5 limits the precision of core–seismic integration, precluding correlation to internal reflectivity within unit S3 (Fig. 3d).

Distribution and volume of intra-caldera deposits

Using our extensive dataset of reflection seismic data, we trace the seismic units throughout the caldera to map out their bases and thicknesses on the scale of seismic resolution (~5 m) (Fig. 4a–f). Velocity measurements of the cores enable the two-way time intervals to be converted to thicknesses in metres, and thus provide the bulk and DRE volumes of each seismic unit (Supplementary Tables 1 and 2). As we cannot trace seismic units underneath Kameni Volcano, we provide minimum volumes that include only the area shown in Fig. 4a–f, whereas the maximum volumes for seismic units S2 and S3 are calculated from interpolation through the Kameni edifice (Fig. 4f and Supplementary Fig. 3). The base of unit S1 is significantly deeper in the northern basin than in the southern basin (Fig. 4a), a manifestation of the pronounced topographic step between the two basins (see Fig. 3c). Unit S1 has a bulk volume of $0.30 \pm 0.04 \text{ km}^3$ ($0.09 \pm 0.01 \text{ km}^3$ DRE) and is slightly thicker in the northern basin (Fig. 4d). Unit S2 thickens significantly towards Kameni Volcano (Fig. 4e), being the thickest between Nea and Palea Kameni (~200 m). Unit S2 has a bulk volume of $2.0 \pm 0.7 \text{ km}^3$, translating to a DRE volume of $0.53 \pm 0.18 \text{ km}^3$ (Fig. 4e). The base of unit S3 forms a deep (~280 mbsf) subcircular depression in the northern basin (Fig. 4c), filled by the deposits of unit S3 (Fig. 4f), which have a bulk volume of $2.65 \pm 0.75 \text{ km}^3$ ($1.30 \pm 0.37 \text{ km}^3$ DRE).

Origin of the acoustic basement

The incoherent acoustic basement underlying seismic units S1–S3 was not penetrated during IODP Expedition 398. No deposits from the Minoan eruption were recovered in any of the intra-caldera cores

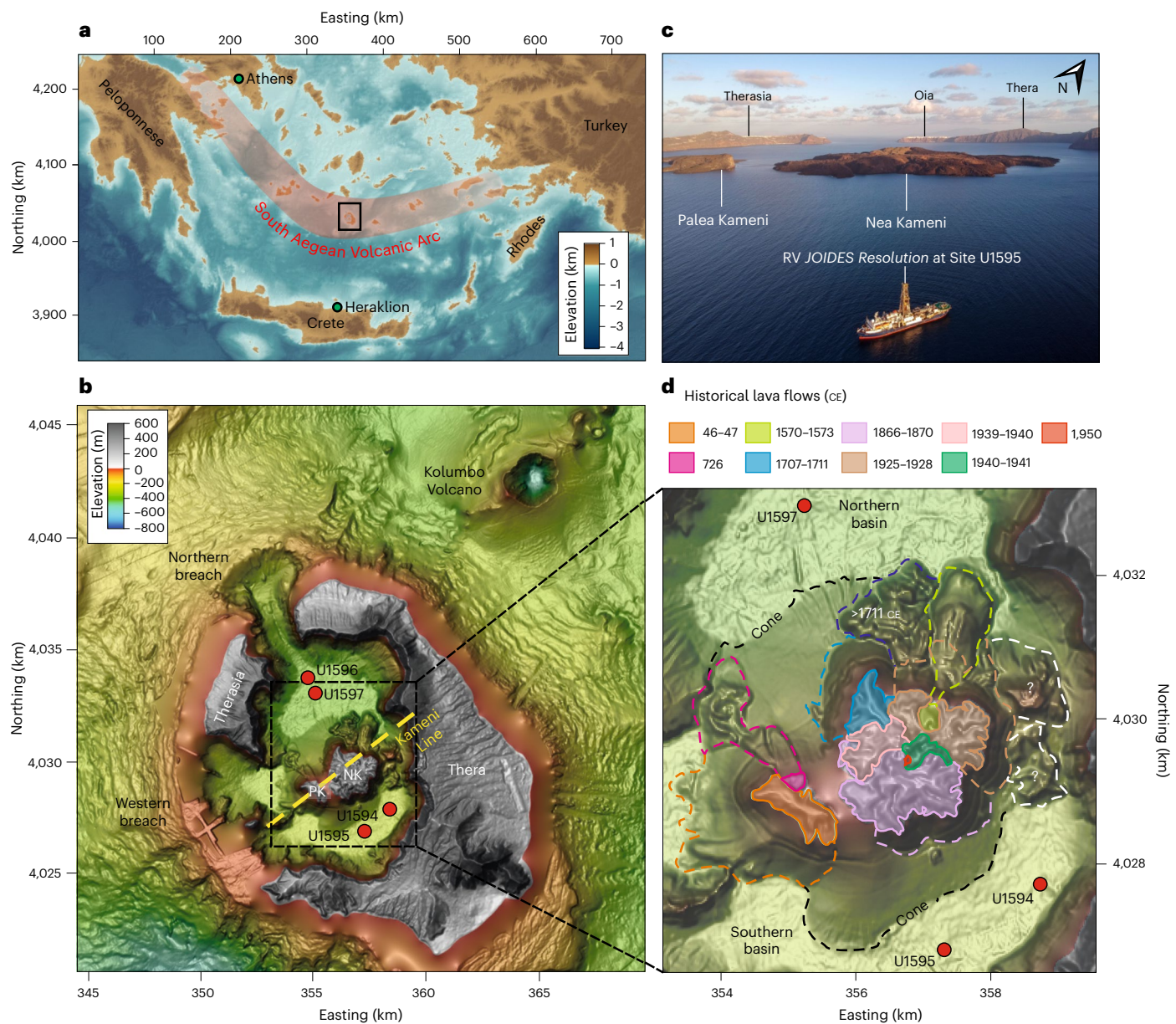


Fig. 1 | Morphology of the Santorini caldera and Kameni Volcano. **a**, Regional map of the southern Aegean Sea showing the South Aegean Volcanic Arc (shaded red). The black box marks the study area. Green circles mark major cities on the coast of the Aegean. The coordinate system here and in subsequent maps is UTM Zone 35 N, WGS84 datum. **b**, Morphological map of the Santorini caldera¹⁶, showing the drill sites (red circles). The dashed yellow line indicates the Kameni Line, a volcano–tectonic lineament defined by the linear alignment of post-Minoan vents. NK, Nea Kameni; PK, Palea Kameni. **c**, Aerial photo of the Santorini caldera with the drilling vessel *JOIDES Resolution* positioned at the

foreground. **d**, Enlargement from **b** of the Kameni Volcano with dated onshore lava flows in semi-transparent colours bounded by solid lines at present-day sea level¹⁰. Outlines of the offshore continuation of lava flows are marked by dashed lines¹¹. The black dashed line (labelled ‘Cone’) indicates the outline of proposed submarine talus deposits¹¹. White dashed lines indicate lava flows of unknown ages, and the dark blue dashed line indicates a lava flow with an age between 1711 and 1925 CE¹¹. Uninterpreted versions of **b** and **d** are included in Supplementary Fig. 1.

(Figs. 2 and 3a). Internal reflections of unit S3 lie subparallel to the acoustic basement and show no indications of significant internal faulting (Fig. 3d,e), which would be expected if unit S3 was deposited before or during caldera collapse¹³ (Fig. 3e). The seismic profile shown in Fig. 3c strikes parallel to the caldera wall in the southern basin (Fig. 3c). The locations of distinct ridges of the acoustic basement in the seismic data (Fig. 3c) correspond to the edges of morphologically fresh landslide scars in the caldera walls of the southern basin (Fig. 3f), formed by rotational landslides during or soon after the Minoan eruption²³. In the northern basin, the acoustic basement forms a deep sub-circular depression (Figs. 3e and 4c) that overlies a cylindrical low-velocity P-wave anomaly, which was identified in a previous seismic

tomography experiment²⁴ (Fig. 4d–f). In both basins, internal reflections of unit S3 overlap the acoustic basement (Fig. 3d,e), implying that seismic unit S3 post-dates the Minoan collapse.

Ages of intra-caldera deposits

Historical documents provide descriptions of 9 effusive to mildly explosive eruptions of Kameni Volcano since 197 BCE^{15–17} (Fig. 5a). The distribution and ages of lava flows of Nea Kameni are well documented^{15,16}. The ages of Palea Kameni lavas are inferred from historical descriptions¹⁷ and, following previous authors^{15,16}, we accept these ages for this study. To relate these eruptions to the recovered lithologies and seismic units, we explore the offshore continuation of onshore

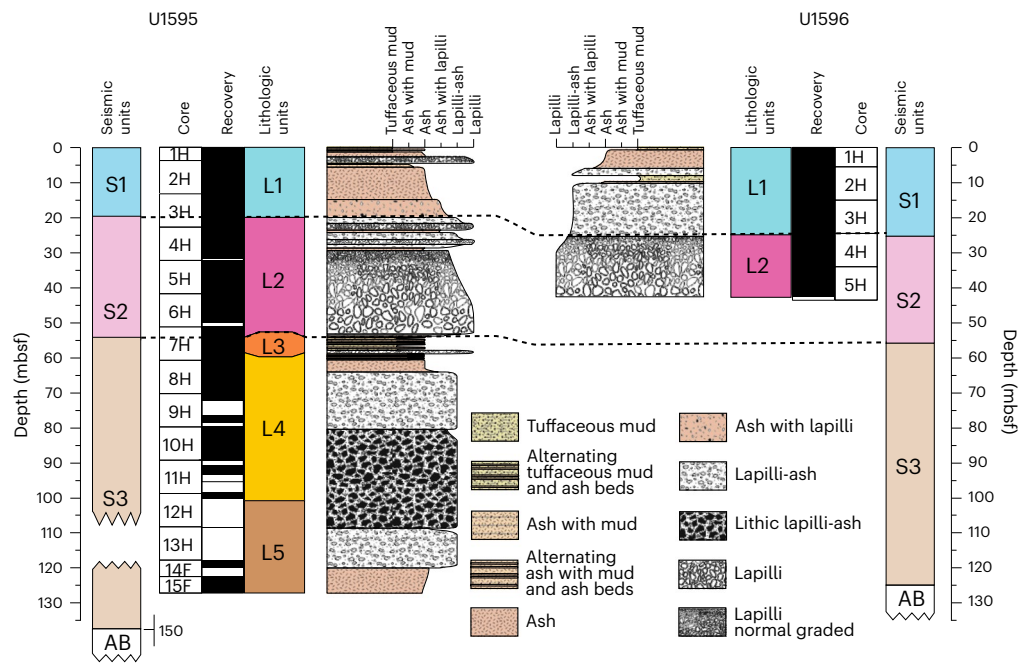


Fig. 2 | Generalized lithostratigraphy of the intra-caldera deposits. Depth of seismic units S1–S3 with the corresponding core names, recovery, lithologic units and lithostratigraphic profiles for Sites U1595 and U1596. Black areas in the recovery column indicate complete recovery, and white areas indicate recovery gaps. AB, acoustic basement.

lava flows¹⁶ (Fig. 1d). Figure 5b shows a three-dimensional (3D) view of two seismic profiles combined with an inset showing the topographic grid. This figure highlights how the subaerial parts of the 46–47 CE (orange), 726 CE (magenta), 1707–1711 CE (light blue) and >1711 CE (dark blue) lava flows extend into the offshore domain¹⁶ and how they relate stratigraphically to the intra-caldera pyroclastic units (Fig. 5b). Each of these lava flows correlates with laterally confined subunits in the seismic profiles, characterized by a high-amplitude top reflection and a chaotic internal seismic character that is typical of submarine lava flows²⁵ (Fig. 5b). Unit S2 lies between the lava flows of the 726 CE and 46–47 CE eruptions (Fig. 5b–d and Extended Data Figs. 1 and 2), which implies that unit S1 post-dates 726 CE. Unit S2 has an age between 47 and 726 CE, and unit S3 pre-dates 47 CE (Fig. 5a).

Origin of intra-caldera deposits

Between the Minoan caldera collapse and the 46–47 CE eruption of Palea Kameni (Fig. 5a,b), only one eruption (197 BCE) is mentioned in historical accounts, which formed an island that was submerged via subsequent erosion¹⁷. Our seismic data indicate the presence of buried lava flows at the boundary between seismic units S2 and S3 in both basins, which may correlate with the 197 BCE eruption (Figs. 3c and 5b–d and Supplementary Fig. 3c). Lithologic unit L3 lies directly at the boundary of seismic units S2 and S3, where the buried lava flow pinches out (Fig. 3c–e). It comprises several intervals of intercalated ash and tuffaceous mud (Figs. 2 and 3a), which may correspond to ancient eruptions of Kameni Volcano. Below, large parts of unit S3 consist mostly of lithic sands and gravels (lithologic unit L4) that may have been deposited through either collapses of the unstable caldera walls, stream flow in the newly formed caldera or flooding when the northern rim of the caldera was breached²¹ (Fig. 5c). Lithologic unit L5 contains volcanic material and may represent an early phase of Kameni Volcano, potentially older than 197 BCE.

Seismic unit S2 consists entirely of pumice and ash (Fig. 3a), and the absence of intercalated muds implies that it formed during an uninterrupted eruption (Figs. 2 and 3). Historical accounts mention that, during the summer of 726 CE, the sea within the Santorini caldera

began to boil until dense smoke rose and was accompanied by pyroclastic eruptions¹⁷. Subsequently, large pumice blocks were ejected in such quantity that they covered the sea over an immense area, reaching the coasts of Macedonia and Asia Minor more than 400 km away¹⁷. These events may have prompted Emperor Leo III of Constantinople to impose iconoclasm, causing severe conflicts in Byzantine society^{26,27}. Despite the apparent abundance of floating pumice, no substantial deposits from this eruption have been found previously, except for a thin pumice layer (<1 m) overlying the lavas of 46–47 CE on Palea Kameni^{28,29}. Our study indicates that an additional $2.0 \pm 0.7 \text{ km}^3$ of these deposits lie buried inside the caldera, effectively reconciling historical accounts with scientific evidence. The caldera-filling nature of these deposits suggests emplacement by gravity flows accompanied by the fallout of water-saturated pumice through the water column³⁰. Despite a significant intra-caldera thickness, the 726 CE tephra has never been recognized on Santorini, suggesting that the eruption was mostly confined to the submarine realm.

Previous studies have suggested that the vent of the 726 CE eruption was between Nea Kameni and Palea Kameni²⁹, which agrees with our mapping of unit S2 (Figs. 4b,e and 5b). A distal ash layer of Kameni origin (0.4 km^3 DRE), with an estimated age between 200 and 950 CE, has been identified in marine sediments up to 41 km east of Santorini^{7,31}. Similar glass compositions indicate a correlation of the distal ash with unit L2 and the onshore Kameni compositional field of the 726 CE eruption (Extended Data Fig. 4). This ash probably represents the late stage of the eruption when the vent became subaerial, which has been suggested in historical descriptions¹⁷ and agrees with the seismic interpretation (Fig. 5b–d), where the offshore continuation of the 726 CE lava flow lies on top of unit S2. Adding the distal ash to our estimated intra-caldera volume of unit S2 indicates a bulk volume of up to 3.1 km^3 and a DRE volume of $\sim 1 \text{ km}^3$ for this eruption, implying an eruption magnitude of volcanic explosivity index (VEI) 5, of the same order of the 2022 Hunga Tonga–Hunga Ha’apai eruption³². Unknown quantities of pumice transported in rafts and deposited across the Aegean seafloor further increase this volume³³.

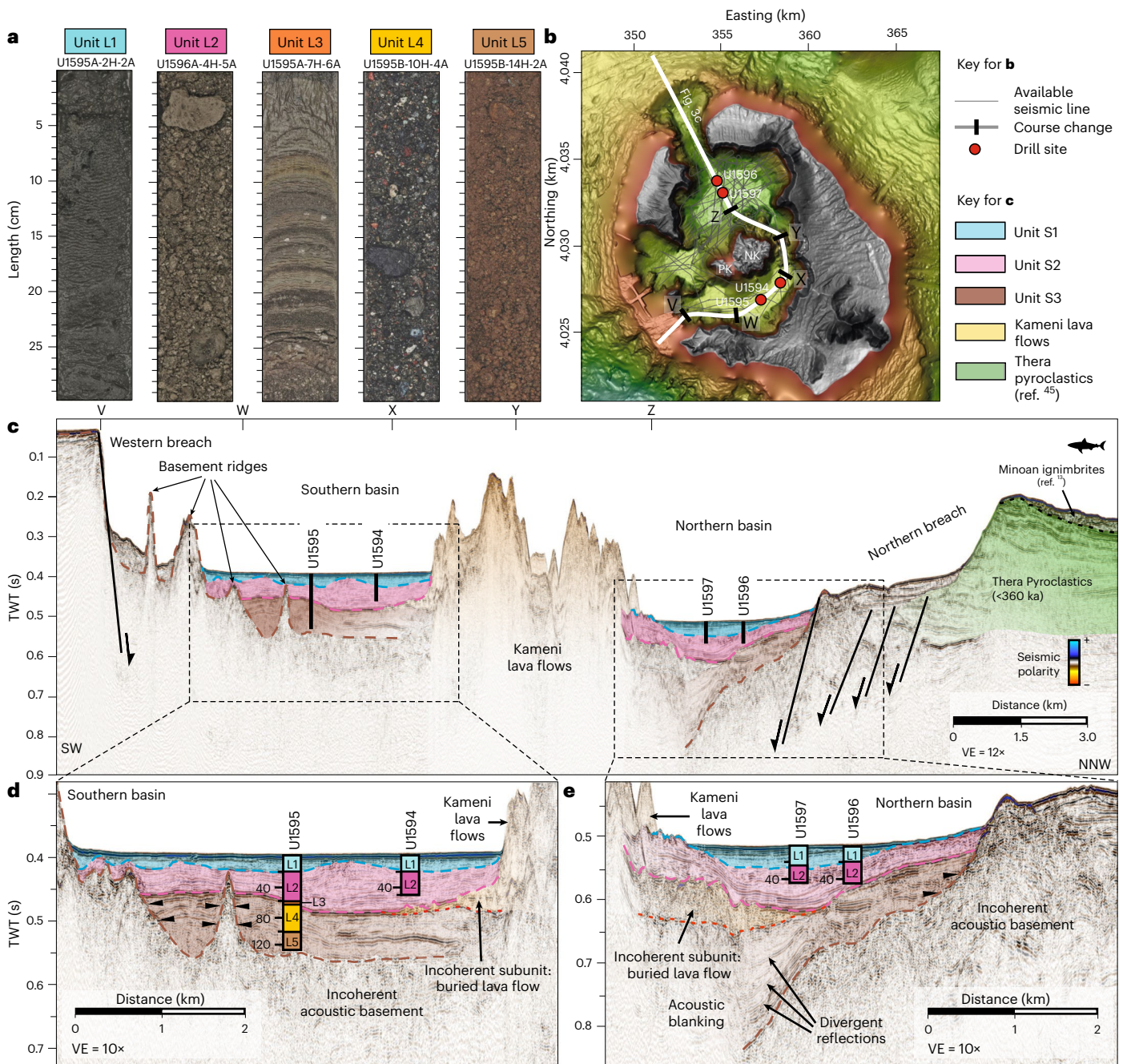


Fig. 3 | Core-seismic integration of the intra-caldera sites. a, Representative photos of the five lithologic units L1–L5. **b**, Overview map with all available seismic profiles in the caldera (grey) and the location of the seismic profile shown in **c**. The labelled black markers (V–Z) indicate course changes of the seismic profile. **c**, Seismic profile crossing the Santorini caldera from the western breach across the southern and northern basins towards the northern breach^{13,45}. Labelled black lines (V–Z) mark the course changes of the seismic profile. For location, see **b**. TWT, two-way travel time; VE, vertical exaggeration.

d, e, Enlargement of the seismic image in **c** of the southern basin (**d**) and northern basin (**e**) with subseafloor depths of the lithologic units L1–L5. Black arrowheads indicate onlap terminations against the acoustic basement. Numbers on the core graphics represent the depth in metres below seafloor. Brown dashed lines indicate the outline of the acoustic basement; red dashed lines indicate the approximate base of interpreted lava flows. Uninterpreted versions of **c–e** are included in Supplementary Fig. 2. Additional seismic profiles across the caldera are provided as Extended Data Figs. 1–3.

The most recent phase of the evolution of the Santorini caldera is characterized by the eruptions of Nea Kameni, which took place after 726 CE (Fig. 5a). These mainly effusive eruptions shaped the present-day morphology of Nea Kameni and occurred between 1570 and 1950 CE²⁸. The 0.3 km³ volcaniclastic deposits of unit S1 probably correspond to these eruptions (Figs. 2 and 3a), whereas the occurrence of a metre-thick lapilli interval and a decimetre-thick ash interval within unit L1 shows that some of these eruptions were also explosive (Fig. 2).

Implications for hazard assessment

Our study reveals the nature of the marine deposits of an island arc caldera and how they relate to a recharging intra-caldera volcano. Our results demonstrate that Kameni Volcano has been capable of producing a major VEI 5 explosive eruption in the recent past. This changes the prevailing view that Kameni Volcano has been in a predominately effusive state since the Minoan eruption¹⁴ and implies that the Santorini volcanic system has been capable of producing highly explosive eruptions in its current early stage in the caldera cycle.

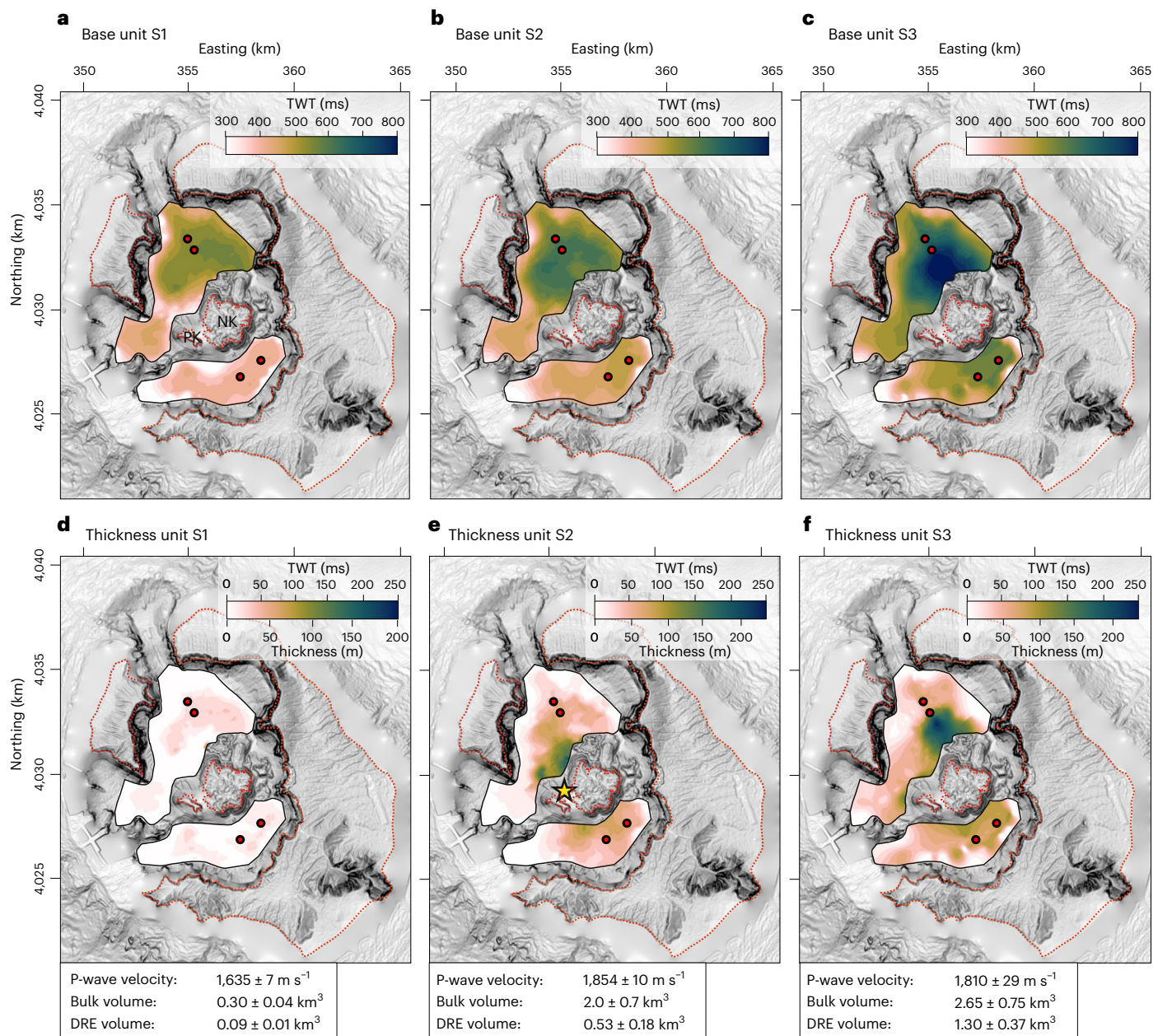


Fig. 4 | Distribution and volume of intra-caldera deposits. **a–f**, Maps of the bases (**a–c**) and thicknesses (**d–f**) of seismic units S1–S3. Seismic units S1 and S2 correlate with lithologic units L1 and L2, and seismic unit S3 includes lithologic units L3–L5. Red dots indicate the locations of the IODP drill sites. Red dotted

lines indicate coastlines. In **e**, the star marks the potential vent location of the 726 CE eruption²⁹. See Supplementary Fig. 3 for a map showing the seismic profiles used for mapping.

Although historical records described the extent of the 726 CE eruption¹⁷, traces of this event were limited to a thin pumice layer on Palea Kameni²⁹. Previous volcanic hazard assessments considered the 726 CE eruption as a worst-case eruptive scenario for Santorini^{34,35} but assumed a significantly smaller eruption magnitude (VEI 3–4) than our study shows^{34,35}. Pumice from the 726 CE eruption may have travelled across the Aegean Sea reaching the coasts of Asia Minor^{17,26}. A similar eruptive event today would have severe consequences not only for the inhabitants of Santorini and its neighbouring islands but also for the broader eastern Mediterranean⁶. Eruption phenomena may include tsunamis generated by submarine explosions, extensive pumice rafts and large airborne ash plumes with significant impacts on coastal communities, aviation, maritime transportation and submarine cables³⁶.

In addition to explosive eruptions, sector collapses are another major hazard for marine volcanoes, as demonstrated by the catastrophic collapses of Mount Mayuyama in 1792 CE³⁷, Ritter Island in 1888 CE³⁸ and Anak Krakatau in 2018 CE³⁹. Similar to Anak Krakatau, Kameni Volcano developed on a topographic step in a flooded caldera⁴⁰. This step corresponds to the Kameni Line, a northeast–southwest-directed active volcano–tectonic lineament²⁴. To the northwest, Kameni Volcano lies on the edge of a subcircular depression that lies at -280 mbsf (Figs. 3c and 4c) and coincides with the focus of 2011–2012 ground deformation^{18,24}. Our study indicates that significant parts of the submarine cone of Kameni Volcano consist of the unconsolidated pumice and ash deposits from the 726 CE eruption (Fig. 5b–d). The lava flows of Nea Kameni were emplaced on top of the up-to-20° steep slopes of these deposits²¹ (Fig. 5b), making the volcano

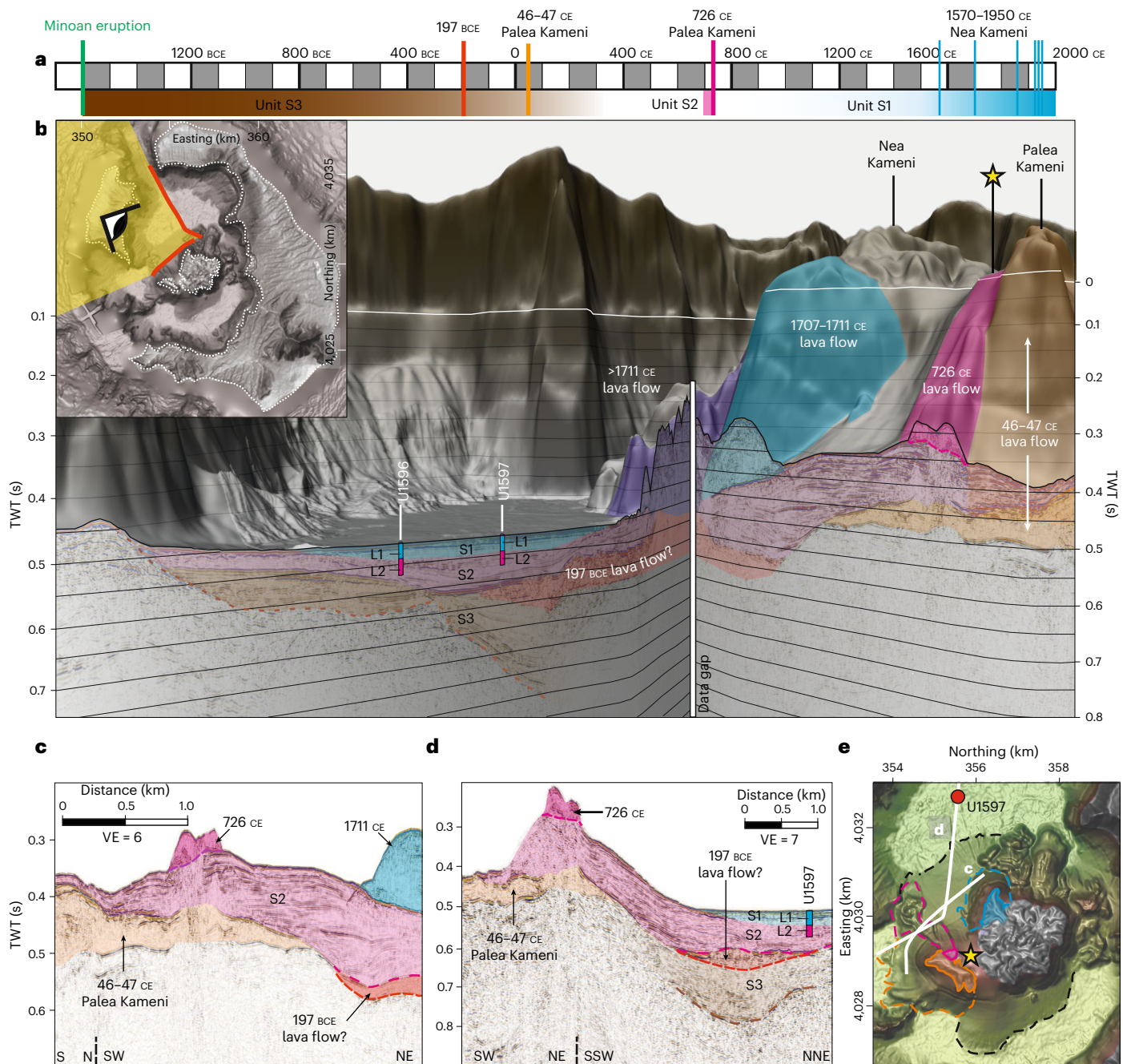


Fig. 5 3D view of the Santorini caldera revealing the relationship between Kameni lava flows and the caldera infill. **a**, Timeline of the post-Minoan evolution of the Santorini caldera. **b**, Two crossing seismic lines combined with an inset showing the topographic model of the Santorini caldera and the Kameni edifice from a vantage point at Therasia. Colours indicate seismic units and lava flows¹⁶. The star marks the potential vent location of the 726 CE eruption²⁹. The solid white line indicates the sea level. The dashed brown line indicates the

acoustic basement. **c,d**, Seismic profiles crossing the northern flank of Palea Kameni and Nea Kameni (**c**) and crossing the northern flank of Palea Kameni and Site U1597 (**d**). **e**, Map of the Kameni edifice with the location of the seismic lines shown in **c** and **d**. The orange, magenta and blue lines show the extent of the 46–47 CE, 726 CE and 1711 CE lava flows, respectively. Uninterpreted versions of **b–d** are included in Supplementary Figs. 4 and 5.

prone to flank instability. Volcanic slope failure occurred during the 1650 CE eruption of Kolumbo Volcano 7 km northeast of Santorini (Fig. 1b), contributing to tsunamis on the neighbouring islands^{41,42}. A comparable flank collapse of Kameni Volcano should be considered a potential hazard scenario for the region.

Our findings stress the need for the monitoring of shoreline crossing and early warning strategies for Santorini, with more than 15,000 residents and more than 2,000,000 tourist visitors each year⁴². Santorini is one of the best-studied marine volcanoes in the world⁸,

yet the presence of vast amounts of pumice within the caldera from a historical Kameni eruption has remained unrecognized until now. This highlights the incompleteness of onshore eruption archives for explosive submarine eruptions. Our study raises the question as to whether other recharging silicic calderas have also been unexpectedly explosive, which has important implications for hazard assessments. Understanding the past and present behaviour of active calderas is key to forecasting their future behaviour and is crucial for assessing regional and global eruption risk^{43,44}.

Online content

Any methods, additional references, Nature Portfolio reporting summaries, source data, extended data, supplementary information, acknowledgements, peer review information; details of author contributions and competing interests; and statements of data and code availability are available at <https://doi.org/10.1038/s41561-024-01392-7>.

References

1. Miller, C. F. & Wark, D. A. Supervolcanoes and their explosive supereruptions. *Elements* **4**, 11–15 (2008).
2. Forni, F., Degruyter, W., Bachmann, O., De Astis, G. & Mollo, S. Long-term magmatic evolution reveals the beginning of a new caldera cycle at Campi Flegrei. *Sci. Adv.* **4**, eaat9401 (2018).
3. de Maisonville, C. B., Forni, F. & Bachmann, O. Magma reservoir evolution during the build up to and recovery from caldera-forming eruptions – a generalizable model? *Earth Sci. Rev.* **218**, 103684 (2021).
4. Kilburn, C. R., Carlino, S., Danesi, S. & Pino, N. A. Potential for rupture before eruption at Campi Flegrei caldera, Southern Italy. *Commun. Earth Environ.* **4**, 190 (2023).
5. Barker, S. J. et al. Taupō: an overview of New Zealand's youngest supervolcano. *N. Z. J. Geol. Geophys.* **64**, 320–346 (2021).
6. Fabbro, G. N., McKee, C. O., Sindang, M. E., Eggins, S. & de Maisonville, C. B. Variable mafic recharge across a caldera cycle at Rabaul, Papua New Guinea. *J. Volcanol. Geotherm. Res.* **393**, 106810 (2020).
7. Kutterolf, S. et al. The medial offshore record of explosive volcanism along the central to eastern Aegean Volcanic Arc: 2. Tephra ages and volumes, eruption magnitudes and marine sedimentation rate variations. *Geochem. Geophys. Geosyst.* **22**, e2021GC010011 (2021).
8. Druitt, T. H. et al. Santorini volcano. *Geol. Soc. Lond. Mem.* **19**, 165 (1999).
9. Vespa, M., Keller, J. & Gertisser, R. Interplinian explosive activity of Santorini volcano (Greece) during the past 150,000 years. *J. Volcanol. Geotherm. Res.* **153**, 262–286 (2006).
10. Druitt, T. H. et al. Magma storage and extraction associated with plinian and interplinian activity at Santorini caldera (Greece). *J. Petrol.* **57**, 461–494 (2016).
11. Druitt, T. et al. Giant offshore pumice deposit records a shallow submarine explosive eruption of ancestral Santorini. *Commun. Earth Environ.* **5**, 24 (2024).
12. Druitt, T. H., McCoy, F. W. & Vougioukalakis, G. E. The Late Bronze Age eruption of Santorini volcano and its impact on the ancient Mediterranean world. *Elements* **15**, 185–190 (2019).
13. Karstens, J. et al. Revised Minoan eruption volume as benchmark for large volcanic eruptions. *Nat. Commun.* **14**, 2497 (2023).
14. Satow, C. et al. Eruptive activity of the Santorini Volcano controlled by sea-level rise and fall. *Nat. Geosci.* **14**, 586–592 (2021).
15. Pyle, D. M. & Elliott, J. R. Quantitative morphology, recent evolution, and future activity of the Kameni Islands volcano, Santorini, Greece. *Geosphere* **2**, 253–268 (2006).
16. Nomikou, P. et al. The emergence and growth of a submarine volcano: The Kameni islands, Santorini (Greece). *GeoResJ* **1**, 8–18 (2014).
17. Fouqué, F. *Santorin Et Ses Éruptions* (G. Masson, 1879)
18. Parks, M. M. et al. From quiescence to unrest: 20 years of satellite geodetic measurements at Santorini volcano, Greece. *J. Geophys. Res. Solid Earth* **120**, 1309–1328 (2015).
19. Sakellariou, D. et al. Seismic stratigraphy of Santorini's Caldera: a contribution to the understanding of the Minoan eruption. In *Proc. 10th Hellenic Symposium on Oceanography & Fisheries* 1–9 (2012).
20. Johnston, E. N. et al. Stratigraphic relations of Santorini's intracaldera fill and implications for the rate of post-caldera volcanism. *J. Geol. Soc.* **172**, 323–335 (2015).
21. Nomikou, P. et al. Post-eruptive flooding of Santorini caldera and implications for tsunami generation. *Nat. Commun.* **7**, 13332 (2016).
22. Druitt, T., Kutterolf, S. & Höfig, T. W. *Expedition 398 Scientific Prospectus: Hellenic Arc Volcanic Field* (International Ocean Discovery Program, 2022).
23. Druitt, T. H. & Francaviglia, V. Caldera formation on Santorini and the physiography of the islands in the late Bronze Age. *Bull. Volcanol.* **54**, 484–493 (1992).
24. Hooft, E. E. E. et al. Seismic imaging of Santorini: subsurface constraints on caldera collapse and present-day magma recharge. *Earth Planet. Sci. Lett.* **514**, 48–61 (2019).
25. Reynolds, P., Holford, S., Schofield, N. & Ross, A. Three-dimensional seismic imaging of ancient submarine lava flows: an example from the southern Australian margin. *Geochem. Geophys. Geosyst.* **18**, 3840–3853 (2017).
26. Higgins, M. D. Magma dynamics beneath Kameni volcano, Thera, Greece, as revealed by crystal size and shape measurements. *J. Volcanol. Geotherm. Res.* **70**, 37–48 (1996).
27. Treadgold, W. T. *A History of the Byzantine State and Society* (Stanford Univ. Press, 1997).
28. Fytikas, M., Kolios, N., & Vougiouklakis, G. Post-Minoan volcanic activity of the Santorini volcano; volcanic hazard and risk, forecasting possibilities. in *Thera and the Aegean World III* Vol. 2 (eds Hardy, D. A. et al.) 183–198 (Thera Foundation, 1990).
29. Polo-Sánchez, A. et al. Tracking timescales of magma reservoir recharge through caldera cycles at Santorini (Greece). Emphasis on an explosive eruption of Kameni Volcano. *Front. Earth Sci.* **11**, 1128083 (2023).
30. Allen, S. R. & McPhie, J. Products of neptunian eruptions. *Geology* **37**, 639–642 (2009).
31. Kutterolf, S. et al. The medial offshore record of explosive volcanism along the central to eastern Aegean Volcanic Arc: 1. Tephrostratigraphic correlations. *Geochem. Geophys. Geosyst.* **22**, e2021GC010010 (2021).
32. Poli, P. & Shapiro, N. M. Rapid characterization of large volcanic eruptions: measuring the impulse of the Hunga Tonga Ha'apai explosion from teleseismic waves. *Geophys. Res. Lett.* **49**, e2022GL098123 (2022).
33. Carey, R. et al. The largest deep-ocean silicic volcanic eruption of the past century. *Sci. Adv.* **4**, e1701121 (2018).
34. Jenkins, S. F. et al. Rapid emergency assessment of ash and gas hazard for future eruptions at Santorini Volcano, Greece. *J. Appl. Volcanol.* **4**, 16 (2015).
35. Vougioukalakis, G. et al. Volcanic hazard assessment at Santorini volcano: a review and a synthesis in the light of the 2011–2012 Santorini unrest. *Bull. Geol. Soc. Greece* **50**, 274–283 (2016).
36. Mani, L., Tzachor, A. & Cole, P. Global catastrophic risk from lower magnitude volcanic eruptions. *Nat. Commun.* **12**, 4756 (2021).
37. Wang, J., Ward, S. N. & Xiao, L. Tsunami Squares modeling of landslide generated impulsive waves and its application to the 1792 Unzen-Mayuyama mega-slide in Japan. *Eng. Geol.* **256**, 121–137 (2019).
38. Karstens, J. et al. From gradual spreading to catastrophic collapse – reconstruction of the 1888 Ritter Island volcanic sector collapse from high-resolution 3D seismic data. *Earth Planet. Sci. Lett.* **517**, 1–13 (2019).
39. Walter, T. R. et al. Complex hazard cascade culminating in the Anak Krakatau sector collapse. *Nat. Commun.* **10**, 4339 (2019).
40. Giachetti, T., Paris, R., Kelfoun, K. & Ontowirjo, B. Tsunami hazard related to a flank collapse of Anak Krakatau Volcano, Sunda Strait, Indonesia. in *Natural Hazards in the Asia-Pacific Region: Recent Advances and Emerging Concepts* Vol. 361 (eds Terry, J. P. & Goff, J.) 79–90 (Geological Society, 2012).

41. Karstens, J. et al. Cascading events during the 1650 tsunamigenic eruption of Kolumbo volcano. *Nat. Commun.* **14**, 6606 (2023).
42. Nomikou, P. et al. SANTORY: SANTORINI's seafloor volcanic observatory. *Front. Mar. Sci.* **9**, 796376 (2022).
43. Self, S. & Gertisser, R. Tying down eruption risk. *Nat. Geosci.* **8**, 248–250 (2015).
44. Cassidy, M. & Mani, L. Huge volcanic eruptions: time to prepare. *Nature* **608**, 469–471 (2022).
45. Preine, J. et al. Spatio-temporal evolution of the Christiana–Santorini–Kolumbo volcanic field, Aegean Sea. *Geology* **50**, 96–100 (2022).

Publisher's note Springer Nature remains neutral with regard to jurisdictional claims in published maps and institutional affiliations.

Open Access This article is licensed under a Creative Commons Attribution 4.0 International License, which permits use, sharing, adaptation, distribution and reproduction in any medium or format, as long as you give appropriate credit to the original author(s) and the source, provide a link to the Creative Commons licence, and indicate if changes were made. The images or other third party material in this article are included in the article's Creative Commons licence, unless indicated otherwise in a credit line to the material. If material is not included in the article's Creative Commons licence and your intended use is not permitted by statutory regulation or exceeds the permitted use, you will need to obtain permission directly from the copyright holder. To view a copy of this licence, visit <http://creativecommons.org/licenses/by/4.0/>.

© The Author(s) 2024

¹Institute of Geophysics, University of Hamburg, Hamburg, Germany. ²GEOMAR Helmholtz Centre for Ocean Research Kiel, Kiel, Germany. ³University Clermont-Auvergne, CNRS, IRD, OPGC, Laboratoire Magmas et Volcans, Clermont-Ferrand, France. ⁴Department of Geology and Geoenvironment, National and Kapodistrian University of Athens, Athens, Greece. ⁵Department of Earth and Planetary Science, University of California, Berkeley, CA, USA. ⁶School of Geography, Geology and the Environment, Keele University, Keele, UK. ⁷College of Earth, Ocean, and Atmospheric Sciences, Oregon State University, Corvallis, OR, USA. ⁸Institut De Physique Du Globe De Paris, Centre National de la Recherche Scientifique (CNRS), Paris, France. ⁹Japan Agency for Marine-Earth Science and Technology, Yokosuka, Japan. ¹⁰International Ocean Discovery Program, Texas A&M University, College Station, TX, USA. ¹¹Department of Geology and Geophysics, Woods Hole Oceanographic Institution, Woods Hole, MA, USA. ¹²School of Natural Sciences/CODES, University of Tasmania, Hobart, Tasmania, Australia. ¹³Geology Department, Western Washington University, Bellingham, WA, USA. ¹⁴School of Geosciences, University of South Florida, Tampa, FL, USA. ¹⁵Lamont-Doherty Earth Observatory, Columbia University, Palisades, NY, USA. ¹⁶Department of Earth and Planetary Sciences, University of California, Riverside, CA, USA. ¹⁷Geophysical Institute, University of Alaska Fairbanks, Fairbanks, AK, USA. ¹⁸Charles University, Faculty of Science, Prague, Czech Republic. ¹⁹Laboratoire des Fluides Complexes et leurs Réservoirs, Université de Pau et des Pays de l'Adour, Pau, France. ²⁰School of Ocean Sciences, China University of Geosciences, Beijing, China. ²¹Faculty of International Resource Sciences, Akita University, Akita, Japan. ²²Department of Geology, Kent State University, Kent, OH, USA. ²³Solid Earth Research Group, National Centre for Earth Science Studies, Thiruvananthapuram, India. ²⁴School of Geology, Aristotle University of Thessaloniki, Thessaloniki, Greece. ²⁵University of Cologne, Institute of Geology and Mineralogy, Cologne, Germany. ²⁶Department of Earth and Planetary Sciences, University of Tennessee, Knoxville, TN, USA. ²⁷School of Geography, Earth and Environmental Sciences, Plymouth University, Plymouth, UK. ²⁸Institute of Marine Biology, Biotechnology and Aquaculture, Hellenic Centre for Marine Research, Heraklion, Greece. ²⁹Institute of Geophysics, University of Texas, Austin, TX, USA. ³⁰School of Earth Sciences, University of Bristol, Bristol, UK. ³¹Graduate School of Science, Kobe University, Kobe, Japan. ³²Institute of Earth Sciences, Academia Sinica, Taipei, Taiwan. ³³Department of Geosciences, National Taiwan University, Taipei, Taiwan. ³⁴Key Laboratory of Submarine Geoscience and Prospecting Techniques, Ocean University of China, Qingdao, China. ✉e-mail: jonas.preine@uni-hamburg.de

Methods

Deep-sea drilling

The IODP Expedition 398 took place from December 2022 to February 2023 onboard the scientific drilling vessel *RV JOIDES Resolution*. It drilled a total of 12 sites in and around the Christiana–Santorini–Kolumbo volcanic field²². The expedition encompassed a standard suite of shipboard physical property measurements carried out on the recovered cores⁴⁶. Comprehensive core logging and description utilized established pyroclastic terminology, accounting for drilling and recovery artefacts such as sediment mixing, shear-induced uparching, brecciation, biscuiting and ash liquefaction.

To obtain the most complete recovery, multiple cores with small offsets of ~50 m at each site were anticipated to close recovery gaps of the first core. However, challenging drilling conditions prevented this for the intra-caldera Sites U1594 and U1597, which were only drilled with a single hole. Three holes were drilled at Site U1595 and two holes were drilled at Site U1596. To combine adjacent holes, stratigraphic correlation was applied, which had the goal of identifying overlapping intervals in adjacent holes and splicing them together to derive the most complete subsurface section. Stratigraphic correlation used core imagery but was primarily based on the physical properties of the recovered cores. Shipboard physical property measurements were conducted on all cores obtained during the expedition (source: <https://iodp.tamu.edu/labs/index.html>). For stratigraphic correlation, we analysed the physical properties measured using the whole round multisensor logger (WRMSL) for magnetic susceptibility and gamma-ray attenuation (GRA), as well as the gamma-ray track for Natural Gamma Radiation intensity. On this basis, we applied shifts to the cores when necessary to establish a composite depth scale. Afterwards, the most representative single continuous sedimentary section was created by splicing intervals from multiple holes.

Bathymetry and seismic data

The digital elevation model (DEM) used in this study was created by combining various data sources. These included satellite-derived Advanced Spaceborne Thermal Emission and Reflection Radiometer (ASTER) data, a community-sourced DEM obtained from the European Marine Observation and Data Network (EMODnet), data collected during the GEOWARN project aboard the *RV Aegaeo* and data from the PROTEUS seismic tomography project acquired on the *RV Marcus G. Langseth*. The lateral resolution of the swath dataset is 20 m, which was obtained using the SeaBeam 2120 20 kHz swath system on the *RV Aegaeo* and the Simrad Kongsberg EM 122 12 kHz multibeam echo sounder on the *RV Marcus Langseth*.

The seismic data used in this study are from four cruises between 2006 and 2019^{47,48}. Single-channel seismic data were acquired in 2006 during the THERA project on the *RV Aegaeo*. As the seismic source, a G pulser with a volume of 10 in³ was used. The general processing comprised simple bandpass filtering (15–500 Hz), de-spiking, predictive deconvolution for the suppression of a strong bubble signal, and spherical divergence correction. To migrate the data, we binned the shot points into a regular spacing of 10 m. After migration, we applied a top mute and white-noise removal. The vertical resolution of these data can be approximated to 8–15 m (using the $\lambda/4$ - or $\lambda/2$ -approximation, where λ is the wavelength) within the shallow sediments (velocity = 1,900 m s⁻¹).

For cruise POS338 with the *RV Poseidon*, a GI pulser was used and operated in true GI mode with a primary (generator) volume of 45 in³ and a secondary (injector) volume of 105 in³. Using a 600 m analogue streamer with 24 channels, we defined a common midpoint (CMP) spacing of 12.5 m. Processing of these data comprised trace editing, simple frequency filtering (10–500 Hz), suppression of a receiver-ghost signal by predictive deconvolution, surface-related multiple elimination as well as spherical divergence correction, pre-stack time migration followed by top muting and white-noise removal. These data

have a main frequency of 60 Hz, indicating a vertical resolution of approximately 8–15 m.

Another dataset was collected in 2015 using a Delta Sparker and a 100 -m-long streamer containing 24 channels. Processing comprised trace editing, simple frequency filtering (100–1,500 Hz), de-spiking, normal moveout correction using a constant velocity (1,500 m s⁻¹) and CMP stacking, as well as post-stack migration (10 m CMP spacing) and white-noise removal. These data have a main frequency of 300 Hz, indicating a high vertical resolution of approximately 2.5–5 m.

During the most recent cruise POS538 in 2019, we acquired seismic data with a much higher lateral resolution (a CMP spacing of ~1.56 m (ref. 47)). As a seismic source, we used a GI pulser that was operated in harmonic mode with primary and secondary volumes of 45 in³. Seismic energy was recorded as multiple concatenated Geometrics GeoEel streamer segments, resulting in active streamer sections ranging from 190 m to 250 m in length. Processing comprised trace editing, simple frequency filtering (15–1500 Hz) and multiple suppression via surface-related multiple elimination. This was followed by spherical divergence correction, time-variant frequency filtering, pre-stack time migration, top muting and white-noise removal. With a main frequency of 125 Hz, the vertical resolution can be approximated to 4–8 m.

The processing of seismic data was done using the VISTA seismic processing software (Schlumberger). Seismic interpretation and mapping used the KingdomSuite software (S&P Global) and Petrel software (Schlumberger). All seismic profiles were combined and homogenized in a consistent interpretation project, and a regional seismo-stratigraphic framework was incorporated^{45,49–51}.

Supplementary Figure 3a,b shows maps of units S1 and S2 interpolated through the Kameni edifice to provide maximum volumes. Supplementary Figure 3c shows the mapped thickness of the proposed lava flow between units S2 and S3. Supplementary Figure 3d shows all seismic profiles used for mapping the intra-caldera deposits. The scientific colour map batlowK used in Supplementary Fig. 3 and Fig. 4 was used in this study to prevent visual distortion of the data and the exclusion of readers with colour vision deficiencies⁵².

Physical property measurements

All four boreholes were integrated with the seismic data to identify key stratigraphic marker horizons using the reservoir characterization software HampsonRussell (GeoSoftware). This was based on shipboard measurements of P-wave velocities and densities of the cores. Continuous P-wave velocities and GRA densities were measured onboard the *RV JOIDES Resolution* using the WRMSL. The sampling for WRMSL measurements was 2.5 cm, with an integration time of 3 s for each measurement. The reliabilities of the WRMSL measurements were assessed by passing a single core liner filled with deionized water through the WRMSL after every core.

The WRMSL compressional wave velocity sensor measured the travel time of 500 kHz ultrasonic waves across the whole core while it remained in the core liner. The waves were transmitted to the core by plastic transducer contacts connected to linear actuators. To ensure coupling between the transducers and the core liner, pressure was applied to the actuators, and water was dripped along the outside of the core liners to enhance the physical connection with the actuators.

The bulk density was calculated by measuring the attenuation of gamma rays as they passed through the core. Ray attenuation is dominated by Compton scattering and depends on the density and thickness of the sample. Gamma rays with an energy of 0.662 MeV are generated using a ¹³⁷Cs source core^{53,54} and pass through the entire diameter of the core. The GRA detector recorded these gamma rays using a 75 × 75 mm sodium iodide detector. The spatial resolution of the GRA is <1 cm.

In addition, discrete P-wave and density measurements were conducted on the working halves of the split cores. For P-waves, entire working halves of split cores were measured with a calliper transducer wetted with deionized water to ensure optimal contact. The sampling

interval was approximately 40–50 cm, depending on the lithologic variability of each core section. For the measurements, Panametrics-NDT Microscan delay line transducers at 500 kHz were used. A total of 925 P-wave velocity measurements from the four intra-caldera sites were conducted.

Volume estimation and DRE conversion

The bulk volumes of seismic units were estimated using shipboard P-wave velocities measured on the recovered cores. The DRE conversion factor quantifies the volume of magma erupted in comparison with the deposit volume, after eliminating all pore space from vesicles and intergranular voids. To determine this conversion factor, several measurements are taken from samples obtained through coring using the moisture and density facilities on the *RV JOIDES Resolution*. These measurements include the water content, bulk density, grain density and solid density.

A dual-balance system, utilizing two Mettler-Toledo XS204 analytical balances, was used to measure wet and dry masses. One balance served as a reference, while the other measured the unknown mass, compensating for ship motion. Before weighing sample-standard pairs, the balances were ‘tared’ to zero based on the average of 300 measurements, with this process repeated every 6 h. Standard weights, similar in value to the sample’s weight, were placed on the reference balance, while the sample was placed on the balance for measuring the unknown mass. The reported sample mass represents the average of 300 measurements. If the reference and sample masses differed by more than 2 g, the measurement was aborted and repeated after adjusting the weights on the reference balance. Typically, the wet samples range from 10 to 20 g.

Following sample collection, the wet sample mass was immediately measured. The dry sample mass and volume were determined after drying the samples in a convection oven at a temperature of 105 ± 5 °C for 24 h, followed by cooling in a desiccator for 3 h. The dry volume was measured using a shipboard helium-displacement pycnometer with a precision of ± 0.04 cm³. Each volume value represents the average of three measurements. These measurements were utilized in the calculation of sediment properties and subsequent determination of the DRE conversion factor.

Calculation of the sediment bulk density, dry density, grain density, porosity and void ratio followed the conventional ODP/IODP approach, assuming a porewater salinity of 0.035 ml⁻¹ and a density of 1.024 g cm⁻³. The presence of isolated vesicles entirely enclosed by glass in pumice clasts can result in the measured grain density being lower than the solid density. To address this, we use the maximum recorded grain density as a proxy for the solid density (2,660 kg m⁻³). Eighty-six moisture and density samples of the caldera deposits were analysed across four sites and seven holes.

Chemical analyses

To decipher the provenance of unit L2 and compare it with other marine tephros we utilized geochemical glass-shard compositions of marine tephros of nearby marine gravity cores as well as the previously established glass-compositional reference data for terrestrial Aegean arc tephros^{7,31} comprising data from deposits of all known eruptions that potentially contribute to the basins in the region of the Christiana–Santorini–Kolumbo volcanic field.

The 63–125 µm fraction of the samples was embedded with epoxy resin into 12 pre-drilled holes in acrylic mounts and polished to facilitate measurements using a JEOL JXA-8200 wavelength-dispersive electron microprobe (with an accelerating voltage of 15 kV, a beam current of 6 nA and a 10-µm-diameter electron beam) at GEOMAR, Kiel for major elements (Supplementary Tables 3–5). Accuracy was monitored via standard measurements on Lipari obsidian and Smithsonian basaltic standard VGA99 (two measurements each after every 60 analyses). To address the effects of variable post-depositional

hydration and minor deviations in focusing of the electron beam, all analyses with totals of >90 wt% were renormalized to 100%.

The trace element contents of glass shards were analysed using LA-ICP-MS (laser ablation inductively coupled plasma mass spectrometry) at the Academia Sinica in Taipei, Taiwan as well as the Laboratory of Magmatism and Volcanism in Clermont-Ferrand, France using 193 nm excimer lasers with beam sizes of 24–30 µm and Agilent 7500 or 7900 ICP-MS instruments (Supplementary Table 6). As internal standards, ⁴³Ca concentrations were used that have been determined using the electron microprobe (CaO oxide contents (in wt%)) on the same glass shard. The external standard was NIST 612 and secondary standard BCR was used as certified reference material. GLITTER (<http://www.glitter-gemoc.com>) software was used to reduce the data and calibrate with standards to obtain trace element concentrations. The analytical precision was better than 10% for most trace elements with limits of detection of <100 ppb for most trace elements and -10 ppb for rare earth elements. Both laboratories resulted in the same trace element concentrations and ratios within analytical uncertainty for the same samples. For further details, the reader is referred to refs. 7,31.

Data availability

The findings of this study are supported by openly available DEM data. In addition, the findings of this study are supported by openly available EMODnet and PROTEUS data, which can be found on the EMODnet bathymetry portal at <https://portal.emodnet-bathymetry.eu>. The hosting of the data is done by the CitationEMODnet Bathymetry Consortium (2018) and can be accessed at <https://doi.org/10.12770/18ff0d48-b203-4a65-94a9-5fd8b0ec35f6>. The high-resolution seismic reflection profiles obtained during POS538 can be accessed at <https://doi.org/10.1594/PANGAEA.956579>.

References

- Blum, P. *Physical properties handbook: a guide to the shipboard measurement of physical properties of deep-sea cores* Technical Note 26 (Ocean Drilling Program, 1997).
- Hübscher, C. et al. Toward a risk assessment of central Aegean volcanoes. *Eos* **87**, 401–407 (2006).
- Karstens, J. et al. POS538: High-resolution 2D and 3D reflection seismic analysis of tsunamigenic volcanic eruptions in the Southern Aegean Sea (Greece) (2021)
- Preine, J. et al. The Hidden Giant: how a rift pulse triggered a cascade of sector collapses and voluminous secondary mass-transport events in the early evolution of Santorini. *Basin Res.* **34**, 1465–1485 (2022).
- Preine, J., Hübscher, C., Karstens, J. & Nomikou, P. Volcano-tectonic evolution of the Christiana–Santorini–Kolumbo rift zone. *Tectonics* **41**, e2022TC007524 (2022).
- Karstens, J. et al. Formation of undulating seafloor bedforms during the Minoan eruption and their implications for eruption dynamics and slope stability at Santorini. *Earth Planet. Sci. Lett.* **616**, 118215 (2023).
- Crameri, F., Shephard, G. E. & Heron, P. J. The misuse of colour in science communication. *Nat. Commun.* **11**, 5444 (2020).
- Evans, H. B. GRAPE* – a device for continuous determination of material density and porosity. In *Proc. SPWLA 6th Annual Logging Symposium (Volume II)* B1–B25 (OnePetro, 1965).
- Harms, J. C. & Choquette, P. W. Geologic evaluation of a gamma-ray porosity device. In *Proc. SPWLA 6th Annual Logging Symposium (Volume II)* C1–C37 (OnePetro, 1965).

Acknowledgements

The samples and data used in this study were provided by the International Ocean Discovery Program (IODP). We express our gratitude to the technical staff of the *RV JOIDES Resolution* for their dedicated efforts in achieving the scientific objectives of

Expedition 398, as well as to all the individuals aboard the ship for contributing to an exceptional experience. We would like to extend special thanks to B. Rhinehart, C. Peng and our colleagues for their invaluable assistance in overcoming numerous challenges, and to K. Petronotis and the leadership of IODP for their support. In addition, we would like to acknowledge the member organizations of IODP for financial support, and the Municipality of Thera for their assistance in expedition preparations. Furthermore, we thank the captains and crews of RV *Poseidon* Expeditions POS338 and POS538. J.P. was supported by the German Research Foundation (Grant Hu698/27). The contribution of T.D. is part of the laboratory of Excellence ClerVolc (Laboratory of Excellence ClerVolc Contribution Number 627).

Author contributions

Conceptualization was by J.P. and J.K. Data curation was by A.B., A.C, A. Morris, A.P., A.W., C.B., C.J., C.H., G.K., H.C., I.M., J.P., K.B.J., K.P., M. Manga, M. McCanta, M.T., O.K., P.N., P.P., R.G., R.J., S.B., S.C., S.D., S.K., T.F.-P., T.R., T.D., Y.Y. and Z.M. Formal analysis was by J.P., A. Metcalfe, G.C., H.-Y.L., J.K., K.-L.W., K.P., M. Manga, S.K. and T.D. Investigation was by A.C., A.P., C.B., I.M., J.P., K.P., M. Manga, M.T., P.N., R.G., R.J., S.B. and S.D. Methodology was by C.H., G.C., J.K., J.P. and Z.M. Project administration was by C.H., P.N., S.K., T.R., T.D. and J.P. Resources were by C.H., P.N., S.K., T.D., J.P. and J.K. Software was by C.H., J.P., G.C. and J.K. Visualization was by J.K., J.P. and S.K. Writing (draught) was by J.P. and J.K. Writing (editing) was by J.K., C.H., S.K., T.D., R.G., C.B., C.J., G.C., G.K., I.M., M. Manga, M.T., S.B. and T.R. Writing (review) was by A.B., A.C, A. Metcalfe, A. Morris, A.P., A.W., C.B., C.J., C.H., D.P.,

G.C., G.K., H.C., H.-Y.L., I.M., J.K., J.P., K.B.J., K.-L.W., K.P., M. Manga, M. McCanta, M.T., O.K., P.N., P.P., R.G., R.J., S.B., S.C., S.D., S.K., T.F.-P., T.R., T.D., X.L., Y.Y. and Z.M.

Funding

Open access funding provided by Universität Hamburg.

Competing interests

The authors declare no competing interests.

Additional information

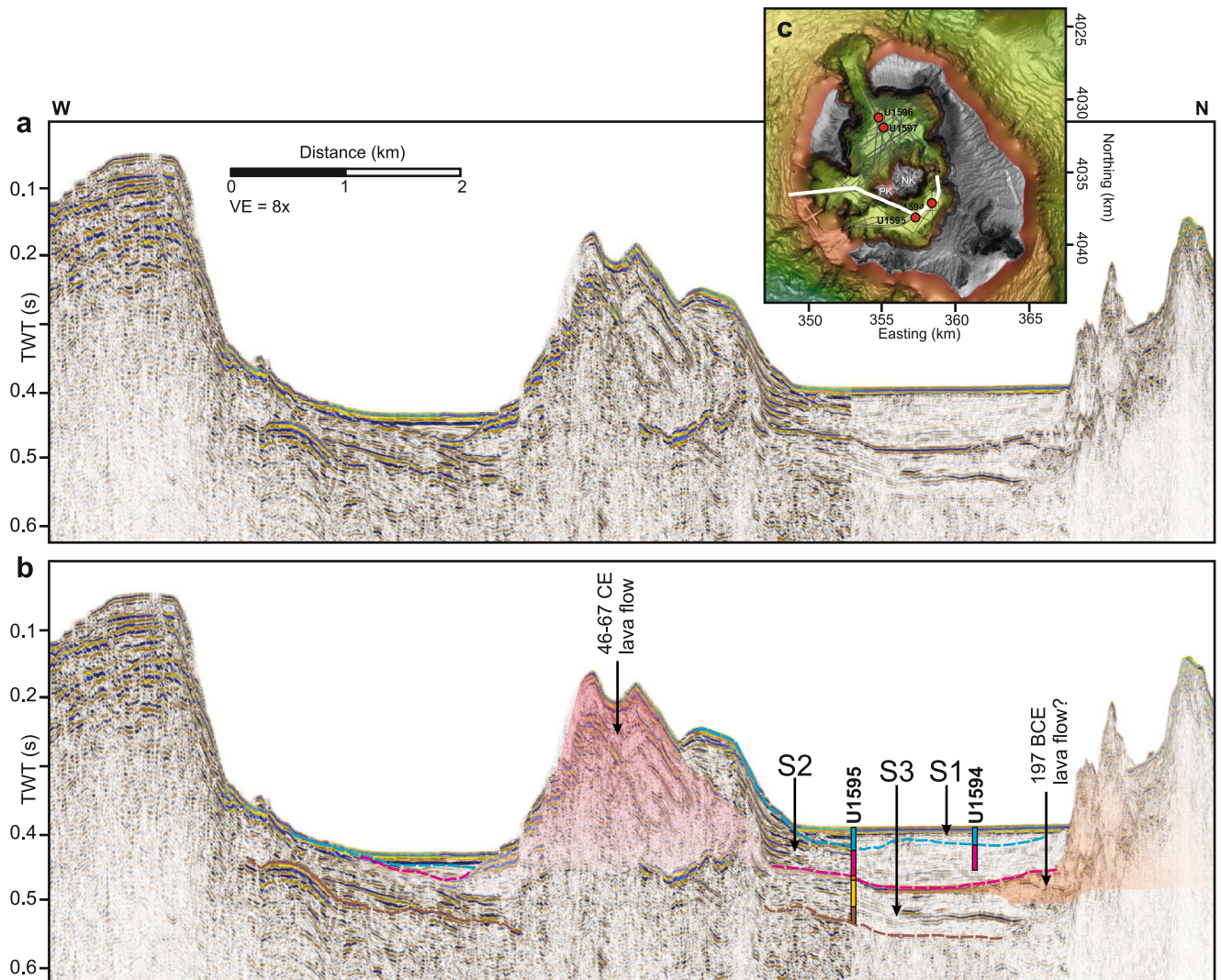
Extended data is available for this paper at <https://doi.org/10.1038/s41561-024-01392-7>.

Supplementary information The online version contains supplementary material available at <https://doi.org/10.1038/s41561-024-01392-7>.

Correspondence and requests for materials should be addressed to Jonas Preine.

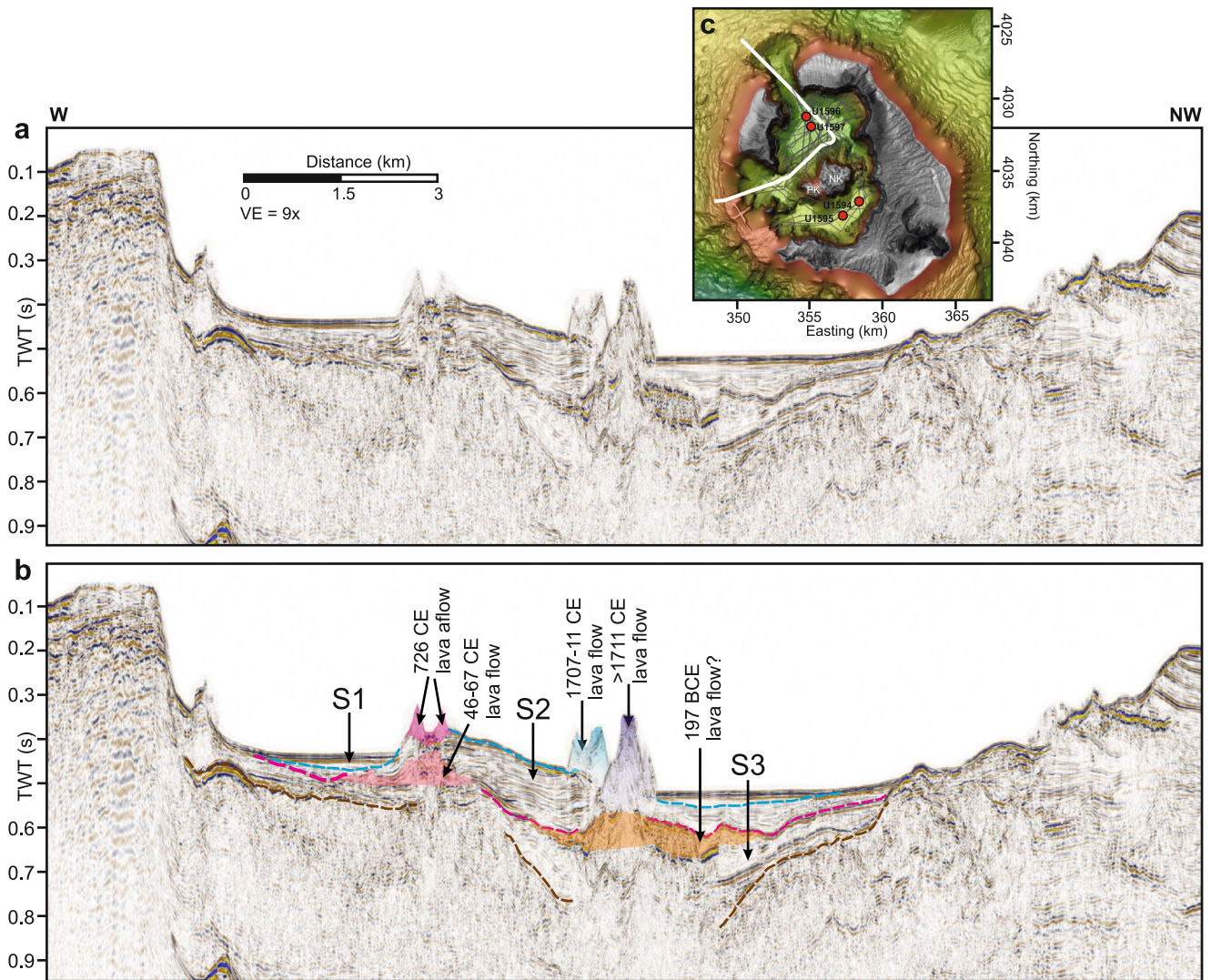
Peer review information *Nature Geoscience* thanks Ben Kennedy, Erik Klemetti and Craig Magee for their contribution to the peer review of this work. Primary Handling Editor: Alireza Bahadori, in collaboration with the *Nature Geoscience* team.

Reprints and permissions information is available at www.nature.com/reprints.

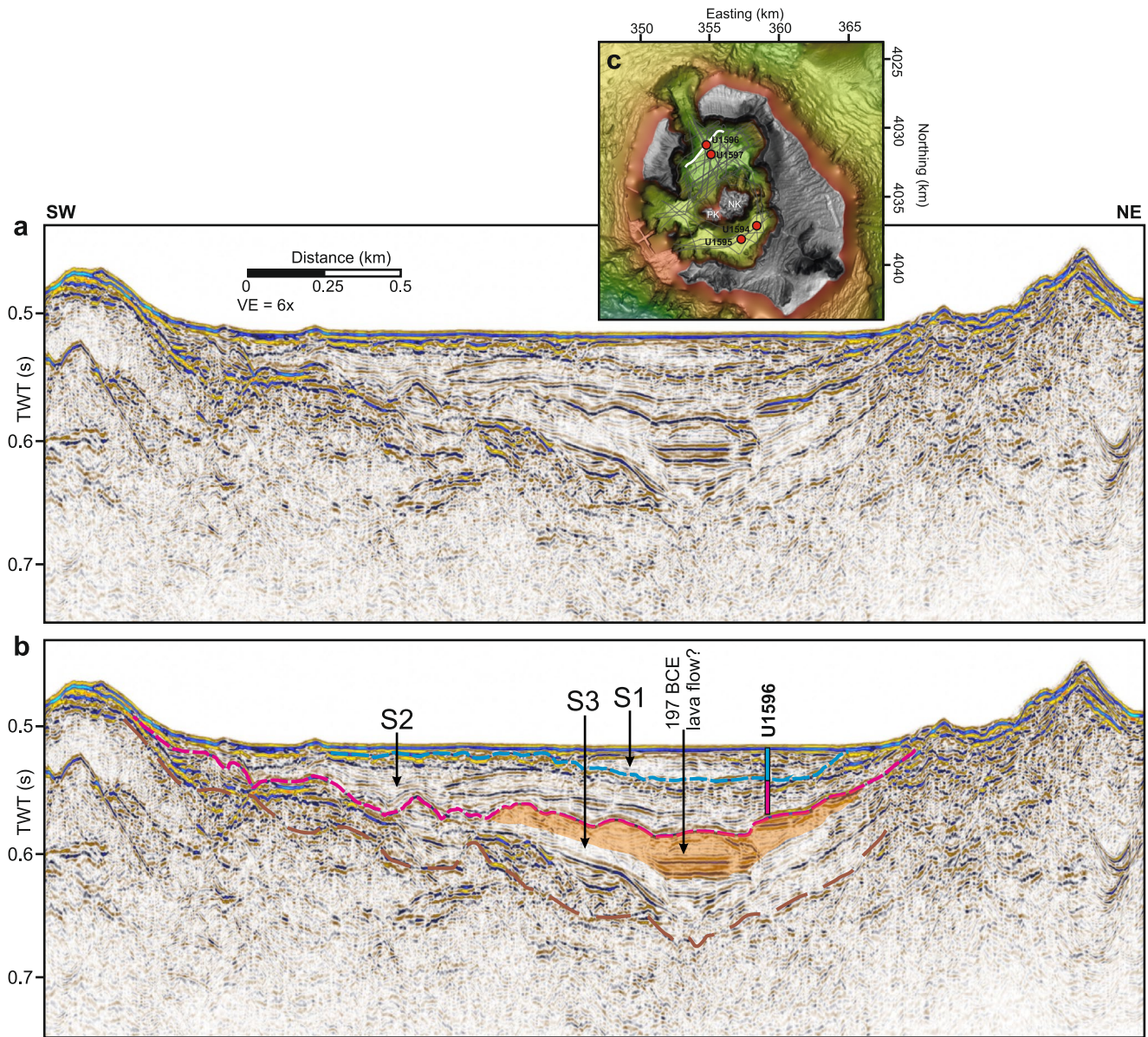


Extended Data Fig. 1 | Seismic profile across the western flank of Kameni volcano and the southern caldera basin. a, b, Un-interpreted (**a**) and interpreted (**b**) version of a seismic profile crossing the western breach, the western flank of the Kameni edifice and the southern caldera basin with Sites

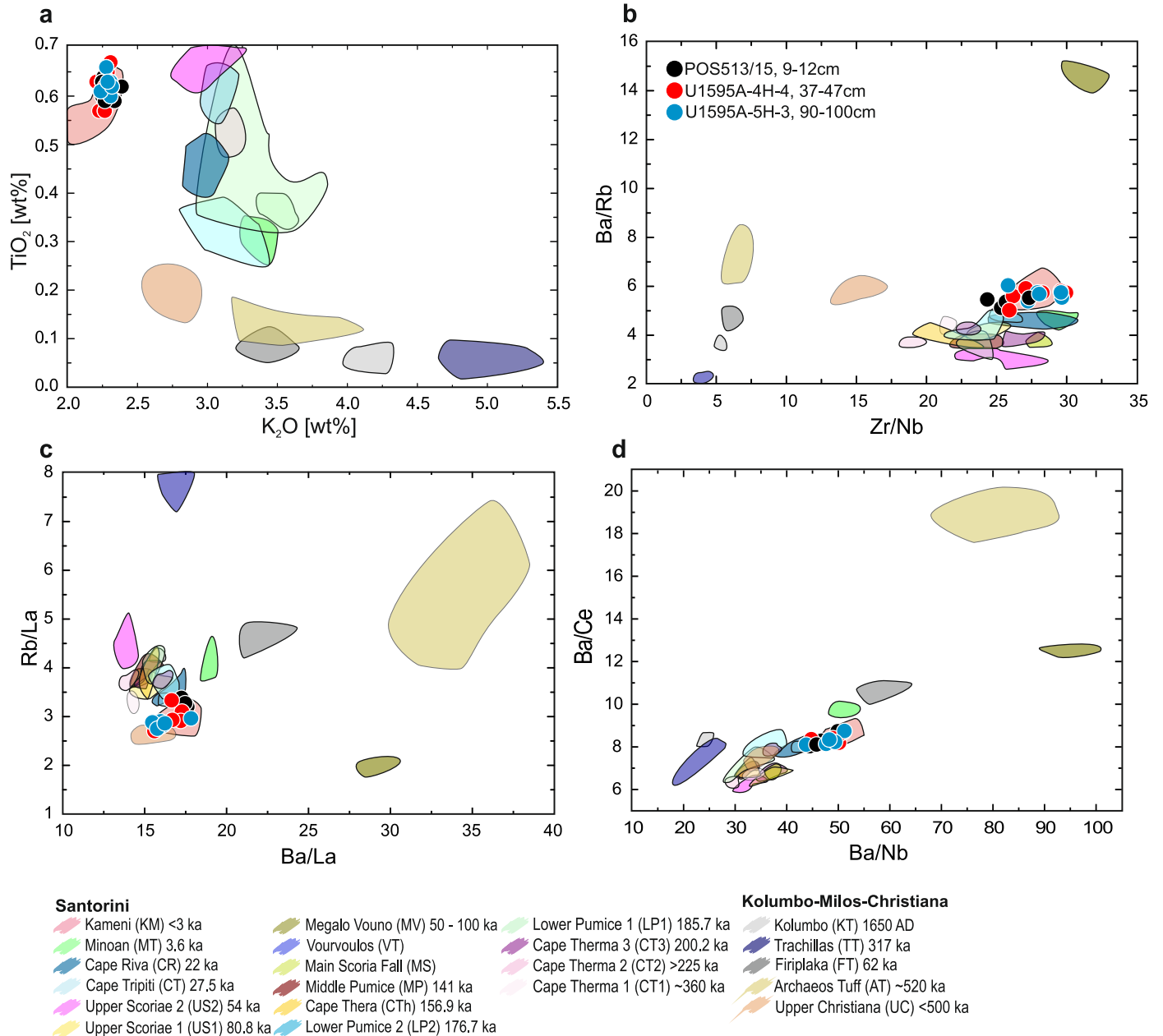
U1595 and U1594. Note that Site U1595 marks the intersection of two seismic profiles acquired with different acquisition parameters, introducing a lateral change in seismic resolution. **c,** Map of Santorini caldera showing the location of the seismic profile in (**a**) and (**b**).



Extended Data Fig. 2 | Seismic profile across the northwestern flank of Kameni volcano and the northern caldera basin. a, b, Un-interpreted (a) and interpreted (b) version of a seismic profile crossing the western breach, the northwestern flank of the Kameni edifice and the northern caldera basin. **c,** Map of Santorini caldera showing the location of the seismic profile in (a) and (b).



Extended Data Fig. 3 | Seismic profile across the northern caldera basin. **a,b**, Un-interpreted (**a**) and interpreted (**b**) version of a seismic profile crossing the northern caldera basin with Site U1596. **c**, Map of Santorini caldera showing the location of the seismic profile in (**a**) and (**b**).



Extended Data Fig. 4 | Chemical compositions of glasses from the 726 Eruption. **a–d**, Trace element ratio plots showing the compositional field of glass-shards of marine ash layers (normalized to 100 wt% anhydrous compositions) recovered in the Anhydros basin within POS513 (core 15) (Kutterolf et al., 2021a,b) as well as from the pumice layer of Unit L2

(U1595A-4H-4; U1595A-5H-3) within the caldera basin compared with glass-compositions from onshore CSK volcanic complex, Milos, and Kolumbo tephra. The legend at the bottom identifies colored composition fields of the onshore/proximal tephras. All analyses correlate with the onshore Kameni compositional field of the 726 CE eruption.